ADVANCES IN ATMOSPHERIC SCIENCES, VOL. 40, MARCH 2023, 337–349

• **Original Paper** •

On the Key Dynamical Processes Supporting the 21.7 Zhengzhou Record-breaking Hourly Rainfall in China※

Peng WEI[1], Xin XU[*1], Ming XUE[1,2], Chenyue ZHANG[1], Yuan WANG[1], Kun ZHAO[1], Ang ZHOU[1], Shushi ZHANG[3], and Kefeng ZHU[3]

[1]*Key Laboratory of Mesoscale Severe Weather/Ministry of Education and School of Atmospheric Sciences, Nanjing University, Nanjing* 210023, *China*

[2]*Center for Analysis and Prediction of Storms and School of Meteorology, University of Oklahoma, Norman, Oklahoma* 73072, *USA*

[3]*Key Laboratory of Transportation Meteorology of China Meteorological Administration, Nanjing Joint Institute for Atmospheric Sciences, Nanjing* 210041, *China*

(Received 8 March 2022; revised 13 May 2022; accepted 24 May 2022)

ABSTRACT

An extremely heavy rainfall event occurred in Zhengzhou, China, on 20 July 2021 and produced an hourly rainfall rate of 201.9 mm, which broke the station record for mainland China. Based on radar observations and a convection-permitting simulation using the WRF-ARW model, this paper investigates the multiscale processes, especially those at the mesoscale, that support the extreme observed hourly rainfall. Results show that the extreme rainfall occurred in an environment characteristic of warm-sector heavy rainfall, with abundant warm moist air transported from the ocean by an abnormally northward-displaced western Pacific subtropical high and Typhoon In-Fa (2021). However, rather than through back building and echo training of convective cells often found in warm-sector heavy rainfall events, this extreme hourly rainfall event was caused by a single, quasi-stationary storm in Zhengzhou. Scale separation analysis reveals that the extreme-rain-producing storm was supported and maintained by the dynamic lifting of low-level converging flows from the north, south, and east of the storm. The low-level northerly flow originated from a mesoscale barrier jet on the eastern slope of the Taihang Mountain due to terrain blocking of large-scale easterly flows, which reached an overall balance with the southerly winds in association with a low-level meso-β-scale vortex located to the west of Zhengzhou. The large-scale easterly inflows that fed the deep convection via transport of thermodynamically unstable air into the storm prevented the eastward propagation of the weak, shallow cold pool. As a result, the convective storm was nearly stationary over Zhengzhou, resulting in record-breaking hourly precipitation.

Key words: extreme rainfall, multiscale processes, orography, barrier jet, low-level mesoscale vortex

Citation: Wei, P., and Coauthors, 2023: On the key dynamical processes supporting the 21.7 Zhengzhou record-breaking hourly rainfall in China. *Adv. Atmos. Sci.*, **40**(3), 337–349, https://doi.org/10.1007/s00376-022-2061-y.

Article Highlights:

- The extreme rainfall in Zhengzhou was produced by a single quasi-stationary storm supported by converging flows from three directions.
- The northerly barrier jet which was in balance with the southerly flow of low-level mesovortex prevented the northward movement of storm.
- The eastward propagation of cold-pool outflow was prevented by low-level easterly inflow which also fed the storm with rich moisture.

1. Introduction

During 17–23 July 2021, a week-long heavy rainfall event occurred in Henan Province, China. Devastating flooding was caused in highly urbanized areas, leading to huge economic losses of over 100 billion RMB and more than 300 casualties; thus, it was a high-impact weather event that

※ This paper is a contribution to the special collection on the July 2021 Zhengzhou, Henan Extreme Rainfall Event.

* Corresponding author: Xin XU
Email: xinxu@nju.edu.cn

drew wide social concern. In particular, between 0800 and 0900 UTC (1600 and 1700 BJT, Beijing time) on 20 July 2021, an extreme rainfall rate of up to 201.9 mm h^{-1} (measured by rain gauge) was observed in Zhengzhou (hereafter, 21.7 extreme rainfall), breaking the hourly precipitation record of 198.5 mm h^{-1} set in August 1975 in China (Ding et al., 1978).

The occurrence of extreme rainfall usually depends on nonlinear interactions between multiscale processes, ranging from large-scale environmental conditions and mesoscale processes that help organize convective storms to storm-scale dynamics and cloud microphysical processes (Ding, 2015; Schumacher, 2017). According to radar observations and the Rapid Update Cycle Version 2 (RUC-2) analysis (Benjamin et al., 2004), Schumacher and Johnson (2005, 2006) found that of all precipitating weather systems, the mesoscale convective system (MCS) was the major producer of extreme rainfall which accounted for about two-thirds of the extreme rainfall events in the United States. Specifically, two common modes of convective organization were revealed for the extreme-rain-producing MCSs. The first type is termed "training line/adjoining stratiform" (TL/AS), which is a linear MCS with cell motion approximately parallel to the convective line. The second common extreme-rain-producing MCS pattern features "back-building/quasi-stationary" (BB) convective cells along a line. The TL/AS MCSs usually form in a very moist, unstable environment on the cool side of a pre-existing slow-moving surface boundary, while the BB MCSs depend more on the mesoscale/storm-scale processes. In both types of MCSs, extreme rainfall most often takes place in the region with repeated passage of convective cells generated upstream, a process commonly known as "echo training" (Doswell III et al., 1996).

There are also many observational and numerical studies of extreme-rain-producing MCSs in China, especially those which occurred in the warm sector of low-pressure systems (e.g., Sun et al., 2019). Previous studies have revealed the importance of a variety of mesoscale/storm-scale processes, such as cold pools, low-level jets, land-sea breezes, mesoscale convective vortices (MCV), boundary layer inertial oscillations, gravity waves, bores, orography, and urbanization, which have greatly advanced the understanding of extreme rainfall generation in China (e.g., Zhang and Zhang, 2012; Luo et al., 2014; Chen et al., 2016; Su and Zhai, 2017; Xu et al., 2017; Zhang et al., 2017; Liu et al., 2018; Zhang et al., 2019, 2020; Abulikemu et al., 2019; Du and Chen, 2019; Xia and Zhang, 2019; Zhang and Meng, 2019; Hua et al., 2020; Wang et al., 2021). For example, Wang et al. (2014) investigated the initiation, maintenance, and properties of convection in an extreme rainfall event observed in the coastal region of South China during the Southern China Monsoon Rainfall Experiment (SCMREX) (Luo et al., 2017). Convective cells were repeatedly triggered on the windward slope of coastal orography in the early stage of the MCS and, in the later stage, along the outflow boundary of the rainfall-induced cold pool. Two scales of training of convective elements were identified, i.e., echo training and band training, which ultimately caused the extreme rainfall. Zhang et al. (2013) examined the extreme rainfall event in Beijing on 21 July 2012. Their results showed that most of the extreme rainfall occurred in the warm sector rather than along the cold front, with the convective cells triggered repeatedly by local orography. Then the back-building convection moved in a manner of echo training along a quasi-stationary linear convective system into Beijing.

Similar to warm-sector heavy rainfall, the 21.7 record-breaking extreme rainfall also occurred in an environment of high equivalent potential temperature (θ_e) and convective instability (see the environmental conditions in section 3.1), with no pre-existing frontal boundary. However, back-building and subsequent training of deep convection were not found in this extreme rainfall event, different from many previous studies of warm-sector heavy rainfall in China. Instead, the extreme rainfall during 0800–0900 UTC was produced by a single convective storm nearly anchored to Zhengzhou, i.e., a quasi-stationary storm. The main purpose of this work is to reveal the mechanisms responsible for the stationarity of the extreme-rain-producing storm in Zhengzhou. A recent numerical study by Yin et al. (2022) proposed a possible dynamical mechanism that emphasizes the importance of a meso-γ-scale vortex surrounded by arc-shaped updrafts. They stated that the extreme-rain-producing storm was maintained by an arc-shaped convergence in the boundary layer caused by the southwesterly flow of the Huang-Huai cyclone west of Zhengzhou. Herein, we find that a northerly barrier jet (e.g., Overland, 1984; Li and Chen, 1998) causing northerly flows towards Zhengzhou also plays an important role in enhancing the low-level convergence in Zhengzhou. The dynamical balances between low-level flows from different directions and the outflow of the rain-induced cold pool are believed to be primarily responsible for the quasi-stationarity of the storm over Zhengzhou during the record-breaking rainfall hour. While none of the mesoscale processes involved is a new discovery, identifying their roles and contributions constitutes the main contribution of this study, as understanding key processes leading to record-breaking events is clearly important.

The remainder of the paper is structured as follows. In section 2, the observations and reanalysis datasets used in this paper are introduced, describing the numerical experiment setup and the Barnes-type filter (Barnes, 1973) employed for scale separation. The environmental conditions of the 21.7 extreme rainfall event are analyzed in section 3.1, while section 3.2 presents the evolution of the MCS according to both radar observation and numerical simulation. Section 3.3 examines the structure of the low-level mesoscale wind fields surrounding the extreme-rain-producing storm in Zhengzhou, focusing on the formation of a barrier jet along the eastern slopes of the Taihang Mountains (THM). A physical explanation is given in section 3.4 for the rainstorm remaining quasi-stationary in Zhengzhou. A discussion and summary are given in section 4.

2. Data and methods

2.1. *Data sets*

The evolution of the 21.7 extreme-rain-producing convective storm was examined using the operational Doppler radar observations at the Zhengzhou station. The quality control processes of the radar reflectivity follow that of Huang et al. (2017) and Zhou et al. (2020). Non-meteorological echoes are first identified and eliminated according to a differential propagation phase shift (Φ_{DP}) and specific differential phase (K_{DP}). Then the attenuation of radar reflectivity is corrected based on the linear relationship between polarimetric parameters. The 0.01° × 0.01° gridded hourly precipitation data provided by the China Meteorological Data Service Center was adopted, which was produced via the merger of the Climate Precipitation Center Morphing technique (Joyce et al., 2004) and rain gauge observations (Shen et al., 2014). Moreover, the environmental conditions of the convective storm were studied utilizing a 6-hourly, 0.25° × 0.25° ERA5 reanalysis product (Hersbach et al., 2020).

2.2. *Numerical simulation*

A convection-permitting simulation was conducted using the Advanced Research Weather Research and Forecasting model (ARW-WRF v4.3, Skamarock et al., 2008). Indeed, it is one of the convection-permitting resolution ensemble forecasts that employed different initial and boundary conditions and used different physics parameterizations for the 21.7 extreme rainfall event (Zhu et al., 2022). While still not perfect, the current simulation best reproduced the overall evolution of the convective system and the extreme hourly rainfall under consideration (see section 3.2) among the ensemble members.

Figure 1a shows the coverage of the model's single domain, which has a horizontal grid spacing of 4 km. There are 51 vertical levels, with the model top placed at 50 hPa. The vertical layer interval varies with height, from about 10 m near the surface, increasing to about 1000 m at the model top. The model's initial conditions were derived from the ERA5 reanalysis, with the model boundary conditions updated hourly. This real-data simulation ran from 1200 UTC on 19 July 2021 and was integrated forward by 48 hours.

For the model physics, the NSSL 1-moment 6-class microphysics scheme (Gilmore et al., 2004) was adopted, along with the Mellor–Yamada Nakanishi Niino (MYNN) 2.5-level planetary boundary layer scheme (Olson et al., 2019), the MYNN scheme for the surface layer, the Unified Noah land surface model (Tewari et al., 2004), and the Rapid Radiative Transfer Model for General circulation models (RRTMG) for longwave and shortwave radiation (Iacono et al., 2008). The parameterization of cumulus convection was turned off, given the 4 km horizontal resolution of the model.

2.3. *Multiscale analysis: scale separation*

Given the multiscale processes involved in the development of convective systems and associated severe weather (e.g., heavy rainfall, hail, and convective high winds; Xu et al., 2015a; Chen et al., 2017; Fu et al., 2018; Luo et al., 2018; Zeng et al., 2019), the Barnes filter was employed to decompose the meteorological fields (e.g., horizontal wind and temperature) into large-, small-, and meso-scale components. The former two were straightforwardly extracted from the model outputs by applying a low-pass and high-pass filter, respectively. Then the mesoscale component was obtained by subtracting the large- and small-scale output from the total. More details regarding implementing a Barnes filter can be found in the appendix of Xu et al. (2017). Figure 1b presents the response functions of the aforementioned Barnes filters. In general, the large-scale denotes the synoptic conditions with spatial scales greater than 1500 km; the peak response of mesoscale occurs at about 500 km, while the small-scale primarily consists of horizontal scales less than 200 km, particularly those smaller than 100 km.

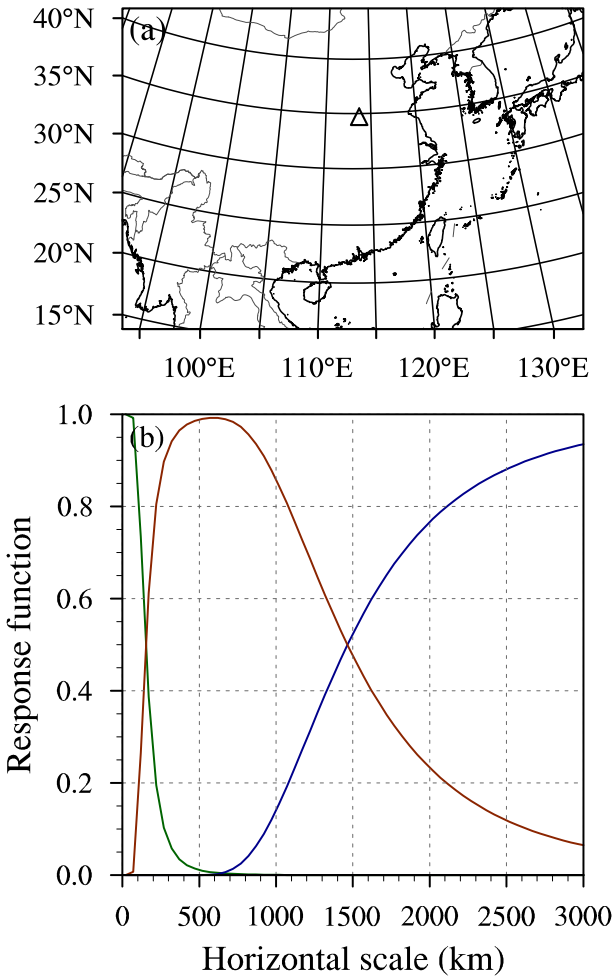

Fig. 1. (a) Geographic location of the model domain. The triangle denotes the location of the radar in Zhengzhou. (b) Response functions of large-scale (blue), mesoscale (orange), and small-scale (green) Barnes-type filters.

3. Results

3.1. *Environmental conditions*

Figure 2 shows the environmental conditions at 0000 UTC on 20 July 2021. The western Pacific subtropical high (WPSH) was mainly located over the Sea of Japan, with the center of the high near 40°N (Fig. 2a). Compared to its 30-yr climatology, the WPSH was displaced abnormally northward by more than 10° in latitude (Zhang et al., 2021). This northward shift of the WPSH was likely caused by Typhoon In-Fa (2021) over the subtropical ocean, which was approaching southeastern China at this time. Abundant water vapor was transported inland from the ocean by the easterlies between the WPSH and Typhoon In-Fa (2021), which turned to southeasterlies/southerlies along the southwestern periphery of the WPSH (Fig. 2b). Due to the blocking of low-level inflow by the THM to the northwest of Zhengzhou (see the topography in Figs. 2a and 2c), as well as the presence of a mesoscale vortex (Fig. 2c) in the vicinity and to the west of Zhengzhou (which was referred to as Huang-Huai cyclone in Yin et al., 2022), there was significant water vapor flux convergence over Zhengzhou, leading to high total column water (TCW) of more than 70 kg m^{-2}

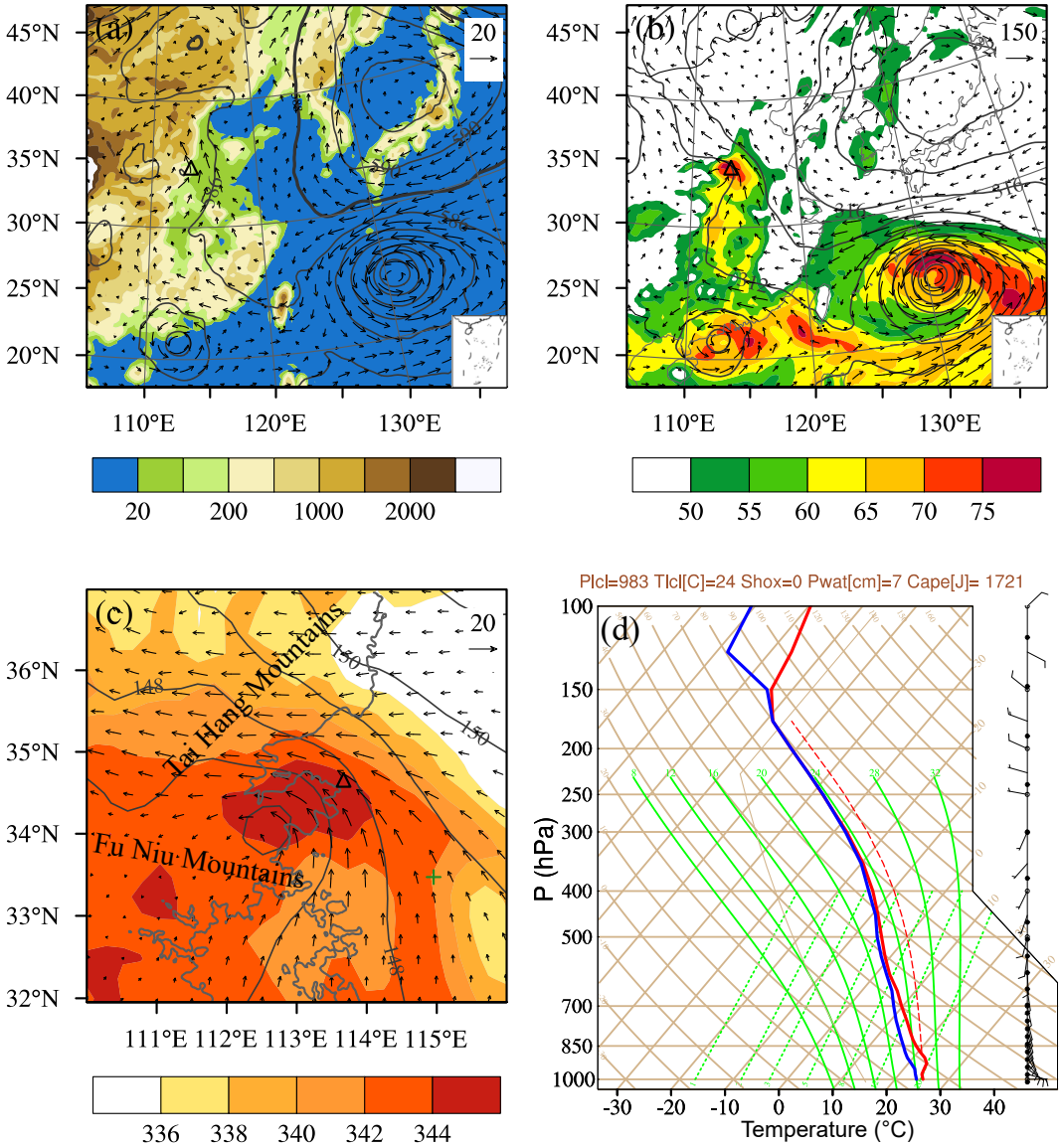

Fig. 2. Environmental conditions derived from the ERA5 reanalysis at 0000 UTC on 20 July 2021. (a) Geopotential height (contours, units: dagpm) and horizontal wind (vectors, units: m s^{-1}) at 500 hPa, with the color shading denoting the topography (units: m). (b) Geopotential height (contours, units: dagpm), total column water (shading, units: kg m^{-2}), and water vapor flux (vectors, units: 10^{-3} kg m s^{-1}) at 700 hPa. (c) Geopotential height (contours, units: dagpm) and equivalent potential temperature (shading, units: K) at 850 hPa. Bold gray lines indicate 200 m terrain height. (d) Skew-*T* diagram for the inflow atmosphere averaged in an area of 1° × 1° centered at the green cross in (c). Red and blue lines denote temperature and dew-point temperature, respectively. The full (half) wind barb represents 4 m s^{-1} (2 m s^{-1}).

(equivalent to 70 mm of precipitable water) (Fig. 2b). This stable, large-scale water vapor supply, similar to what was present during the extreme rainfall that also occurred in Henan province in August 1975 (Ding, 2015), provided favorable moisture conditions for subsequent extreme rainfall (Doswell III et al., 1996).

Benefiting from the transport of warm, moist air from the ocean, Zhengzhou was in a region of high-θ_e (Fig. 2c), indicating sufficient convective instability. Figure 2d shows an atmospheric sounding in the inflow region (to the southeast of Zhengzhou by ~200 km; see the location of the green cross in Fig. 2c) extracted from the ERA5 reanalysis. The troposphere was nearly saturated, conducive to the production of heavy rainfall by preventing the entrainment of dry air (Schumacher and Johnson, 2005). A relatively dry and stable layer was present below about 900 hPa, which was likely a result of surface radiative cooling during the nighttime and early morning. A moderate convective available potential energy (CAPE) of about 1700 J kg^{-1} was found at 0000 UTC, which quickly increased to more than 3200 J kg^{-1} at 0600 UTC (i.e., two hours prior to the extreme rainfall in Zhengzhou) (not shown). The environment inflow veered with height from easterlies to southerlies, with a moderate vertical wind shear of 9.4 m s^{-1} (10.0 m s^{-1}) between 1000–700 hPa (1000–500 hPa). This condition is consistent with previous studies that extreme rainfall often occurs in an environment of weak-to-moderate vertical wind shear throughout the cloud depth (Maddox et al., 1979).

3.2. *Evolution of the MCS*

Figures 3a–3d present the evolution of the convective system from radar observations. Also shown are the horizontal winds and the 850 hPa geopotential height from the ERA5 reanalysis. At 0200 UTC (Fig. 3a), there was an MCS in the Henan province, which can be traced back to at least 0600 UTC on 19 July 2021. Widespread convection was found on the eastern/northeastern flank of the low-level mesoscale vortex, which was a region preferable for convection initiation given the thermodynamic destabilization by vortex-induced isentropic lifting (e.g., Raymond and Jiang, 1990; Trier et al., 2000; Trier and Davis, 2002). In particular, a comma-head echo was apparent on the composite radar reflectivity, which wrapped cyclonically around the vortex center. It is essentially the well-recognized MCS-MCV morphology (e.g., Houze, 2004; Trier et al., 2006). As described below, it is just the southern part of the comma-head echo that caused the extreme rainfall in Zhengzhou during 0800–0900 UTC.

Over time, the low-level mesoscale vortex moved northwestward as it was embedded within the synoptic southeasterly flow, and the MCS moved northwestward accordingly. Two hours later, at 0400 UTC (Fig. 3b), the convection of interest reached the Funiu Mountains (FNM) immediately to the west of Zhengzhou and strengthened, as indicated by the stronger radar reflectivity. The upslope lifting by the FNM played an important role in the organization of the convection (Yin et al., 2022). Furthermore, the insolation at noon remarkably reduced the convective inhibition (CIN) and enhanced the convective instability of the inflow that fed into the convection, as mentioned in section 3.1, which favored the development of intense convection. Notably, a new convective line developed to the west of the convection over the FNM, which was along the eastern/southeastern flank of the low-level mesoscale vortex, a preferable region for the initiation of secondary convection (e.g., Trier and Davis, 2002; Trier et al., 2006; Xu et al., 2017). This convective line intensified over time and became increasingly evident two hours later at 0600 UTC (Fig. 3c). During this time, the convection over the FNM moved further northward, eventually arriving in Zhengzhou at 0800 UTC (Fig. 3d). The convective storm then moved very slowly, producing an extraordinarily heavy rainfall event, exceeding 200 mm between 0800 and 0900 UTC.

Figures 3e–h are similar to Figs. 3a–d but for the evolution of the simulated MCS. In general, the convection-permitting simulation well reproduced the MCS, such as the well-defined comma-head reflectivity that wrapped around the low-level mesoscale vortex, with a long tail trailing southwestward (Fig. 3e). Compared to its observational counterpart, however, the simulated MCS was displaced by a few tens of kilometers to the west and was delayed by about 1 to 2 hours. These timing and positioning biases are common in real-data simulations of MCSs (e.g., Davis and Galarneau, 2009; Meng et al., 2012; Xu et al., 2015b; Abulikemu et al., 2016; Wang et al., 2016). For the simulated MCS, as a whole, it basically moved northwestward in association with the low-level mesoscale vortex. Yet, the southern part of the leading convective line (that eventually caused the extreme rainfall in Zhengzhou) moved northward/northeastward because of the southerly/southwesterly winds of the low-level mesoscale vortex. At 0530 UTC (Fig. 3f), the convection arrived in the FNM and intensified, whereas a secondary convective line began to develop to its west near 112°E. Both were qualitatively consistent with the radar observation. In the next few hours, the simulated convection over the FNM moved further northeastward (Fig. 3g) and reached Zhengzhou at 0900 UTC, i.e., one hour later than reality, with a southward displacement of about 50 km compared to observations (Fig. 3h).

Despite the timing and positioning biases mentioned above, the simulated convective storm also became quasi-stationary in Zhengzhou, producing extremely heavy rainfall of about 160 mm h^{-1}, comparable to the CMORPH precipitation (about 170 mm h^{-1}, Fig. 4). Therefore, it is justified to use this convection-permitting WRF simulation to study the mechanisms responsible for the stagnation of the extreme-rain-producing storm in Zhengzhou.

3.3. *Mesoscale wind and pressure fields*

Figure 5a depicts the simulated horizontal winds at 300 m above the mean sea level (MSL) at 0900 UTC. Three airflows (i.e., easterlies, southeasterlies, and northeasterlies) were found to converge in Zhengzhou and the surrounding regions. The three-way converging flow formed a

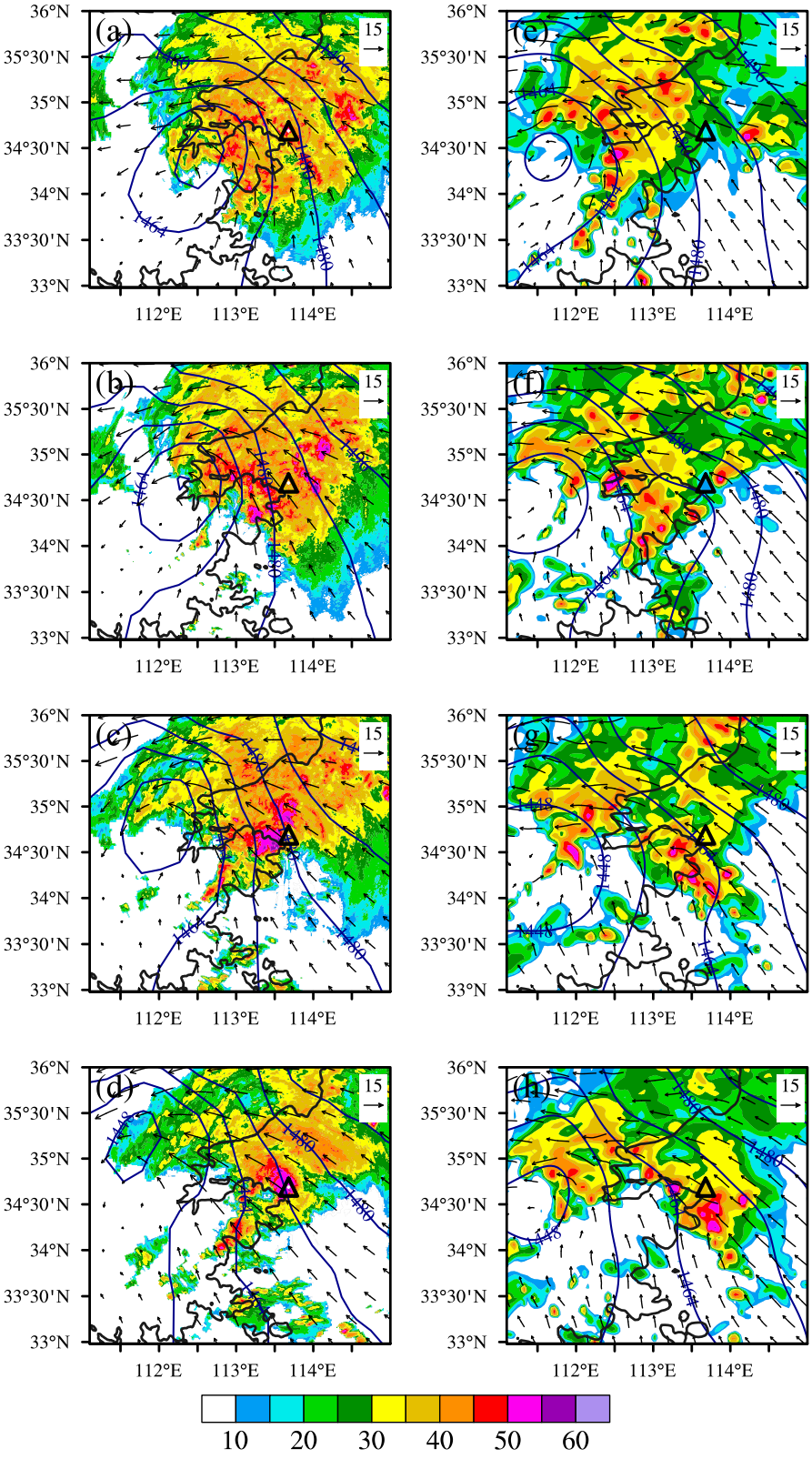

Fig. 3. Observed radar composite reflectivity (shading, units: dB*Z*) and geopotential height (blue lines, units: gpm) and horizontal wind (vectors, units: m s^{-1}) at 850 hPa from the ERA5 reanalysis at (a) 0200 UTC, (b) 0400 UTC, (c) 0600 UTC, and (d) 0800 UTC on 20 July 2021. The right column is the simulated composite reflectivity and geopotential height at (e) 0300 UTC, (f) 0530 UTC, (g) 0730 UTC, and (h) 0900UTC. The small-scale component of geopotential height was filtered in (e)–(f) to better reveal the low-level mesoscale vortex. Gray lines indicate 200 m terrain height.

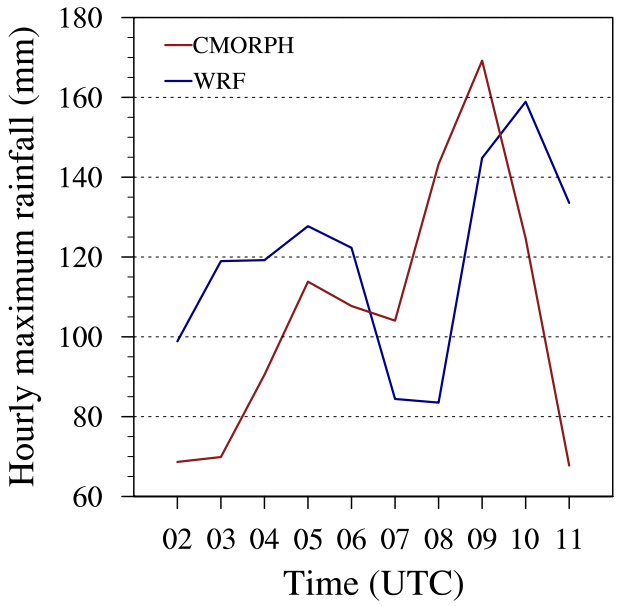

Fig. 4. Time series of the hourly maximum rainfall (mm h^{-1}) in the Zhengzhou area from the CMORPH (red) and the WRF model (blue) from 0200 to 1100 UTC on 20 July 2021.

mesoscale convergence zone centered at the southern tip of the convective storm. (The location of the storm was indicated by the 45-dB*Z* isoline south of Zhengzhou). There were also a few convective-scale features of convergence embedded within this mesoscale region, which were one order greater in magnitude and mainly located on the southern-to-eastern flank of the storm (not shown). Similarly, Yin et al. (2022) also noticed an arc-shaped convergence zone along the south-to-east periphery of the convective storm (see their Fig. 14).

The converging flow pattern was induced by mesoscale winds rather than a large-scale flow, clearly shown after scale separation. The large-scale winds were predominantly southeasterlies in approximate geostrophic balance with the large-scale pressure field (Fig. 5b), indicating little convergence. (The horizontal winds 300 m above MSL were directed slightly toward low pressure due to surface friction.) From the mesoscale fields (Fig. 5c), the convective storm was in a region of obvious horizontal wind convergence, accompanied by negative pressure perturbations in a much broader area than the storm itself. (Hereafter, perturbations are meant as mesoscale components unless otherwise stated.) This meso-β-scale low pressure was caused by a low-level mesoscale vortex in the mountainous areas northwest of Zhengzhou at this time (Fig. 3h). The cyclonic circulation of the low-level vortex resulted in the mesoscale southwesterlies, southerlies, and southeasterlies to the south of the storm. However, to the north of the storm, there were predominantly mesoscale northerly/northeasterly winds, accompanied by positive pressure perturbations, poleward of about 35°N. The high-pressure center adhered to the eastern slope of the THM and gradually decayed to the east (i.e., away from the THM).

Figure 6a shows the wind fields and pressure perturba-

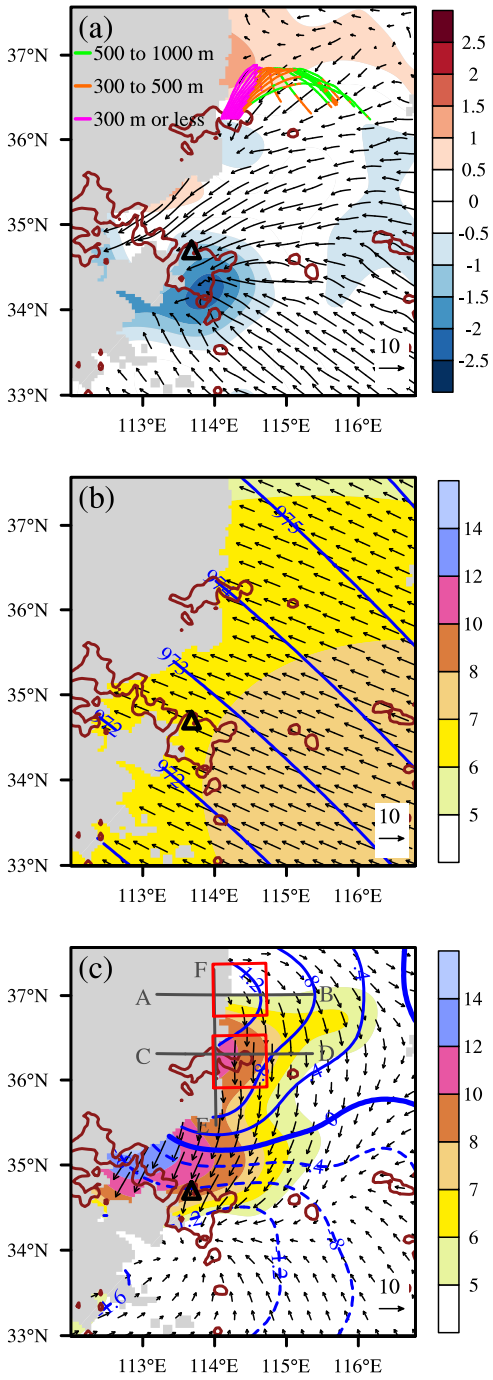

Fig. 5. (a) Simulated horizontal wind (vectors, units: m s^{-1}) and the convergence of mesoscale horizontal winds (shading, units: 10^4 s^{-1}) at 300 m above MSL at 0900 UTC on 20 July 2021. Panels (b) and (c) are similar to (a) but for the large-scale and mesoscale components of the horizontal wind (vectors) and speed (shading, units: m s^{-1}) and pressure (blue contours, units: hPa). Red contours represent the composite reflectivity of 35 dB*Z*. Colored lines in (a) are the 9-h backward trajectories for air parcels terminating at the core region of the barrier jet along the eastern slope of the Taihang Mountains in (c). Lines AB, CD, and EF in (c) indicate the locations of the vertical cross-section shown in Fig. 6. Red boxes in (c) denote the locations where the mesoscale pressure and northerly wind components are calculated in Fig. 7.

tions in the west-east vertical plane along the high-pressure center. The maximum pressure perturbation occurred on the eastern slope (i.e., windward slope, given the prevailing easterly large-scale flow in Fig. 5b) of the THM, which suggested low-level flow blocking by the high terrain of the THM. According to Miranda and James (1992), mountain flow blocking can be measured by the non-dimensional Froude number, namely,

$$\mathrm{Fr}(z) = U(z)/[N(z)(H_\mathrm{m} - z)]\,, \qquad (1)$$

where $U(z)$ is the horizontal wind speed at height z, $N(z)$ is the buoyancy frequency, and H_m is the mountain amplitude. The smaller the Fr, the more the airflow is blocked by the orography. As shown in Fig. 6a, the Fr was less than unity below about 1 km above MSL, reaching as low as 0.25 near the surface. Therefore, significant low-level flow blocking took place east of the THM.

Indeed, low-level blocking emerged as early as 0000 UTC (Fig. 7a). In the early stage, the large-scale easterlies were approximately in geostrophic balance, with the southward-directed pressure gradient force (PGF) balanced by the northward-directed Coriolis force. On approaching the THM, the low-level incoming flow decelerated due to the blocking, leading to a reduction of Coriolis force which was thus overwhelmed by the PGF. Consequently, the quasi-geostrophic easterly flow was forced to turn left, producing an ageostrophic northerly wind component parallel to the THM. This pattern can be readily confirmed by the Lagrangian backward trajectories of parcels within the core region of the northerly flow shown in Fig. 5a. These parcels were

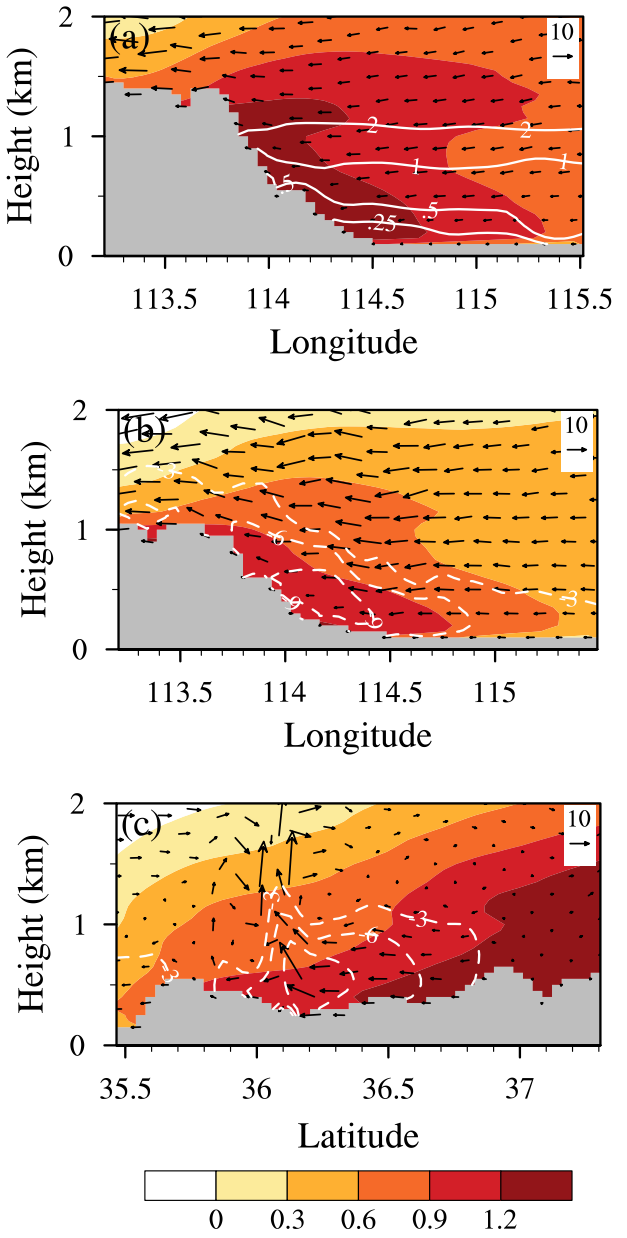

Fig. 6. (a) Simulated in-plane wind fields (vectors, units: m s^{-1}) and mesoscale pressure (shading, units: hPa) in the west-east cross-section along line AB in Fig. 5c at 0900 UTC on 20 July 2021. Vertical velocity (units: m s^{-1}) is exaggerated by 10 times for clarity. Panels (b) and (c) are the same as (a), but for the vertical cross-sections along lines CD and EF in Fig. 5c. White contours in (a) denote the Fr, while they represent the northerly wind component (units: m s^{-1}) in (b) and (c).

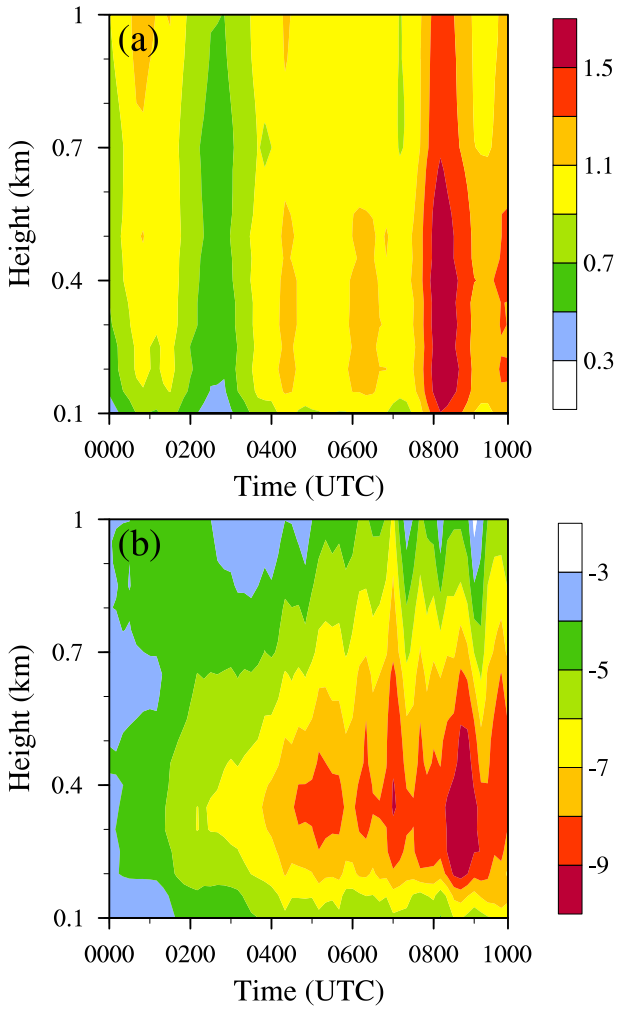

Fig. 7. Time series of the simulated mesoscale (a) pressure (shading, units: hPa) and (b) northerly wind components (shading, units: m s^{-1}) at low levels averaged in the top box and the bottom box in Fig. 5c, respectively.

released at 0900 UTC and traced backward for nine hours. The trajectories were calculated using the model output at 5-min intervals, based on the fourth-order Runge-Kutta scheme adopted in Xu et al. (2017) and Hua et al. (2020).

Given the persistent airflow blocking and the resulting blocking high, the northerly winds accelerated with time (Fig. 7b), forming a barrier jet stronger than 10 m s^{-1} at 0900 UTC along the eastern slope of the THM (Fig. 6b). The jet core was located close to, but south of, the high-pressure (Figs. 5c and 6c). The barrier jet extended away from the THM by about 72 km (as outlined by the 7 m s^{-1} contour), which agrees very well with the Rossby radius of deformation, i.e., $L_R = U/f \approx 71$ km. Here, the large-scale horizontal wind speed and Coriolis parameter were $U = 6.2$ m s^{-1} and $f = 8.8 \times 10^{-5}$ s^{-1}, respectively, as estimated at point B in Fig. 5c. This scale is often adopted to measure the width of airmass that could be trapped by a mountain (Overland and Bond, 1995). Moreover, the maximum wind speed of the barrier jet occurred at about 500 m above MSL, roughly midway up the mountain crest, also in good agreement with previous studies (e.g., Yang et al., 2017).

On approaching the storm in Zhengzhou, the northerly barrier jet gradually turned northeasterly, with even greater speed in the canyon region northwest of Zhengzhou (Fig. 5c). The further acceleration of the jet was due to the enhanced PGF, owing to the presence of negative pressure perturbations. This low pressure, as mentioned above, was associated with the low-level mesoscale vortex located to the west of Zhengzhou (Fig. 8a). Therefore, the mesoscale barrier jet was deflected westward upon accelerating.

3.4. *On the maintenance and stagnation of the extreme rain-producing storm*

Radar observations showed that a single, quasi-stationary storm produced the extreme hourly rainfall in Zhengzhou, which was faithfully reproduced by the real-data, high-resolution simulations conducted herein, as well as in Yin et al. (2022). Notably, convective back-building and echo training, often observed in extreme rainfall events in China (e.g., Zhang et al., 2012; Wang et al., 2014; Liu et al., 2018), were not found in the present case.

Back building of convection depends largely on the mesoscale/storm-scale processes, in particular through the lifting by a cold pool outflow boundary (Schumacher and Johnson, 2005). The cold pool produced by the 21.7 rainstorm was fairly weak, only about 2–3 K colder than the pre-storm inflow to its southeast (Fig. 8a). A west-east cross-section through the cold pool center showed that the cold pool extended upward by no more than 1 km (Fig. 8b). This weak and shallow cold pool was a natural consequence of the very moist environment (Fig. 2d), indicating that the evaporative cooling of rainfall was suppressed substantially (e.g., Davis and Lee, 2012; Xu et al., 2017). Yin et al. (2022) reported no obvious cold pool in this case either. Nevertheless, the convective storm was still well organized and produced extremely heavy rainfall. As shown in Fig. 5, the storm was surrounded by low-level converging flows from different directions. This low-level convergence dynamically lifted the air parcels, promoted intense updrafts, and thus helped maintain the convective storm.

Interestingly, the northeastward-moving convective storm became quasi-stationary once it reached Zhengzhou. The northward movement of the storm was inhibited by the enhanced northerly flow to the north of the storm. The northerly flow originated from the barrier jet on the eastern slope of the THM, and it was accelerated further by the low-level mesoscale vortex west of Zhengzhou (Figs. 5c and 8a). Figure 9 depicts the evolution of the mean southerly wind component averaged between 0–1 km above MSL to the south of the storm and the mean northerly wind component to its north during 0900–1000 UTC. The low-level southerly wind was largely balanced by its northerly counterpart to the north of the storm, with the former about 2.8 m s^{-1} stronger than the latter. Consequently, the storm only experienced a slight northward movement during this period.

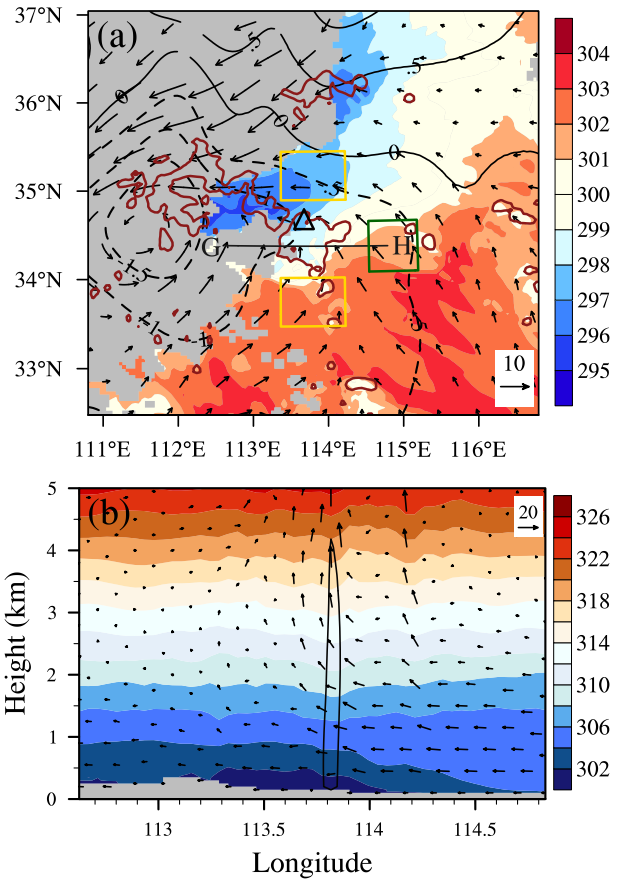

Fig. 8. (a) Simulated temperature (shading, units: K) at 300 m above MSL and mesoscale wind (vectors, units: m s^{-1}) and pressure (contours, units: hPa) at 1500 m MSL at 0900 UTC on 20 July 2021. Red contours are the composite reflectivity of 35 dBZ. (b) Simulated potential temperature (shading, units: K), in-plane winds (vectors), and 45-dBZ reflectivity (black line) in the west-east cross-section along line GH in (a). Vertical velocity (units: m s^{-1}) is exaggerated by 10 times for clarity. The yellow and green boxes denote the locations where the wind speed and easterly inflow are calculated in Fig. 9.

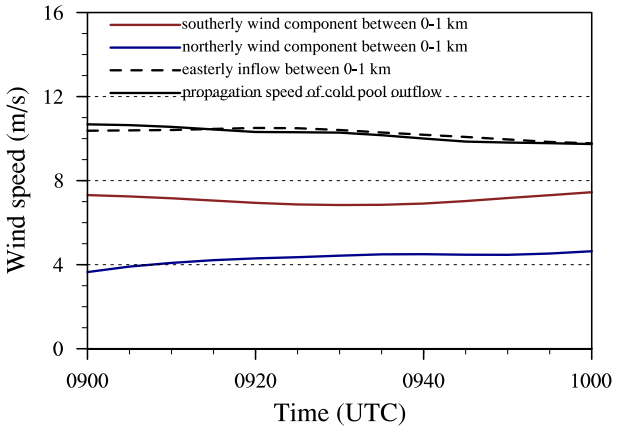

Fig. 9. Evolution of the simulated cold pool propagation speed (solid black, units: m s^{-1}) between 0900 UTC and 1000 UTC on 20 July 2021. Also shown are the simulated mean easterly (dashed black), southerly (red), and northerly (blue) wind components in the low levels (0–1 km), averaged in the green, bottom black, and top black boxes in Fig. 8a, respectively.

As for the west-east direction, the mean easterly wind component to the east of the storm was about 10.2 m s^{-1} (Fig. 9) due primarily to the large-scale flow (Fig. 5). This low-level easterly inflow was nearly completely countered and offset by the westerly outflow of the cold pool. The calculation of the cold-pool outflow speed followed that in previous studies (e.g., Weisman and Rotunno, 2004; Hua et al., 2020):

$$C = \sqrt{2\int_0^H (-B)\mathrm{d}z}\,. \tag{2}$$

Here, H is the cold pool depth, set to 1.0 km, according to Fig. 8b. The buoyancy B is given by:

$$B = g\left[\frac{\theta-\bar{\theta}}{\theta} + 0.61\,(q_\mathrm{v}-\bar{q}_\mathrm{v}) - q_\mathrm{c} - q_\mathrm{r}\right], \tag{3}$$

where θ is the potential temperature and q_v, q_c, and q_r are the mixing ratios of water vapor, cloud water, and rainwater, respectively. The base-state variables indicated by overbars are defined as the areal mean in the near-inflow region (see the green box in Fig. 8a) and temporally averaged between 0900 UTC and 1000 UTC. The approximate balance between the low-level easterly inflow and the westerly outflow of the cold pool led to little eastward movement of the storm. These offsetting zonal flows, in conjunction with the analysis in the north-south direction, help to explain why the convective storm became quasi-stationary in Zhengzhou between 0900 UTC and 1000 UTC.

4. Summary and discussion

On 20 July 2021, heavy rainfall impacted Zhengzhou city in Henan Province, China, with extreme hourly precipitation of up to 201.9 mm occurring between 0800 and 0900 UTC. Based upon radar observations, ERA5 reanalysis, and a real-data WRF simulation with 4-km grid spacing, this work investigated the environmental conditions and evolution of the extreme-rain-producing convective storm, particularly focusing on the mechanisms responsible for the production of the extreme rainfall over the hour.

Results showed that this extreme rainfall event occurred in an environment similar to that of warm-sector heavy rainfall, featuring high temperature and moisture with no pre-existing synoptic frontal boundary. A large amount of warm moist air was transported from the ocean by the easterlies-to-southeasterlies due to Typhoon In-Fa (2021) and the WPSH, the latter of which was abnormally displaced northward. Due to blocking by the Taihang Mountains to the north and a low-level mesoscale vortex west of Zhengzhou, there was notable convergence of low-level momentum and water vapor flux in Zhengzhou and surrounding regions, yielding very favorable conditions for high precipitable water and heavy rainfall. While warm-sector heavy rainfall is often caused by convective back building along the outflow boundary of a rain-induced cold pool and subsequent echo training, interestingly, the 21.7 hourly extreme rainfall was produced by a single, quasi-stationary convective storm. This storm originated from the Funiu Mountains to the southwest of Zhengzhou as part of a convective line that developed on the eastern flank of the low-level mesoscale vortex. Initially, the convective storm moved northeastward due to the steering of the southwesterly flow of the low-level mesoscale vortex but became stagnant in Zhengzhou, where the extreme rainfall occurred.

The overall evolution of the extreme-rain-producing storm was well-captured by a convection-permitting WRF simulation, including the northeastward movement in the early stages and the later stagnation in Zhengzhou. The model results revealed that the northward movement of the convective storm was inhibited by the intensification of a low-level northerly wind component north of Zhengzhou, which was comparable to the southerly wind component associated with the low-level mesoscale vortex. According to scale separation and backward trajectory analyses, this mesoscale northerly flow formed as the larger scale easterly flow impinging on the east-southeast-facing slope of the Taihang Mountain range was blocked, leading to the formation of a southward, terrain-parallel barrier jet. Furthermore, a balance was found between the eastward outflow of the relatively weak precipitation-induced cold pool and the low-level easterly inflow, preventing the storm from moving further east. These low-level flows converged into Zhengzhou from three directions. The combination of low mountains on the west side and an abnormally rich water vapor supply established unusually favorable conditions for the organization and slow movement of sustained deep convection, leading to the record-breaking hourly rainfall over Zhengzhou. These processes are illustrated in a conceptual model given in Fig. 10.

Accumulated rainfall depends on both the rate and duration of rainfall. Heavy rainfall tends to occur in locations

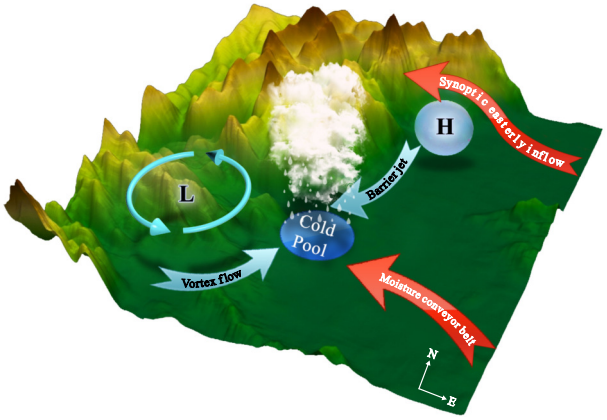

Fig. 10. Schematic diagram illustrating the multiscale dynamical processes responsible for maintaining the 21.7 Zhengzhou extreme rainfall. Synoptic-scale flows are denoted by the thick red arrows, whereas thin blue arrows indicate mesoscale flows. The extreme-rain-producing convective storm was fed by the moisture supply from the ocean (denoted by the red arrow labeled as "moisture conveyor belt") and maintained by the dynamical lifting of low-level converging flows. The northerly flow originated from a mesoscale barrier jet on the eastern slope of the Taihang Mountains, which occurred as the synoptic easterly flow was blocked and formed a blocking high. The southerly flow was associated with a low-level, meso-β-scale vortex west of Zhengzhou. An overall balance was reached between the low-level northerly and southerly winds. Moreover, the easterly inflow prevented the eastward propagation of the rain-induced cold pool. Thus, the convective storm was nearly stagnant in Zhengzhou, resulting in record-breaking hourly precipitation.

where high rainfall rates last for a long time (Doswell III et al., 1996). This work provides insights into how multiscale dynamical processes can work synergistically to keep a convective storm quasi-stationary while at the same time providing strong low-level convergent forcing and consequently produce recording-breaking hourly rainfall. Yet, more detailed studies are still needed to fully understand all processes contributing to the 21.7 hourly extreme rainfall. For instance, Yin et al. (2022) emphasized the significance of a meso-γ-scale vortex. As noted in Nielsen and Schumacher (2020), about half of the hourly extreme rainfall events in the United States were associated with low-level rotation, suggesting that the rotationally-induced, upward-directed dynamic perturbation pressure gradient force can promote an intense updraft and thus potentially enhance the short-term rainfall rate (Nielsen and Schumacher, 2018). However, this finding should be taken with caution. Both Trapp and Weisman (2003) and Xu et al. (2015a) noticed that the low-level rotation could also induce a downward-directed perturbation pressure gradient force that would aid in suppressing convection. Thus, the dynamic impacts of low-level rotation on the organization of such an extreme-rain-producing storm remain to be clarified. Moreover, microphysical processes can also affect quantitive precipitation. Using disdrometer and polarimetric radar observations, Chen et al. (2022) revealed unusually high concentrations of raindrops of all sizes (showing combined properties of both maritime and continental convection), implying that both ice-based and warm rain processes contributed importantly to the high rainfall rate in the present case. Detailed microphysical processes, as well as their possible coupling with dynamic processes that support very high rainfall rates, will be investigated in the future.

Acknowledgements. This work is jointly supported by the National Science Foundation of China (Grant No. 42122036), the Second Tibetan Plateau Scientific Expedition and Research (STEP) program (2019QZKK0105), the National Key R&D Programs of China (2018YFC1507300), the National Science Foundation of China (Grant No. 91837207), and the Beijing Climate Center (QHMS2021008).

REFERENCES

Abulikemu, A., X. Xu, Y. Wang, J. F. Ding, S. S. Zhang, and W. Q. Shen, 2016: A modeling study of convection initiation prior to the merger of a sea-breeze front and a gust front. *Atmospheric Research*, **182**, 10–19, https://doi.org/10.1016/j.atmosres.2016.07.003.

Abulikemu, A., Y. Wang, R. X. Gao, Y. Wang, and X. Xu, 2019: A numerical study of convection initiation associated with a gust front in Bohai Bay region, North China. *J. Geophys. Res.*, **124**, 13 843–13 860, https://doi.org/10.1029/2019JD030883.

Barnes, S. L., 1973: Mesoscale objective map analysis using weighted time-series observations. NOAA Tech. Memo. ERL NSSL-62, National Severe Storms Laboratory, Norman, 60 pp.

Benjamin, S. G., and Coauthors, 2004: An hourly assimilation–forecast cycle: The RUC. *Mon. Wea. Rev.*, **132**, 495–518, https://doi.org/10.1175/1520-0493(2004)132<0495:AHACTR>2.0.CO;2.

Chen, G., and Coauthors, 2022: Variability of microphysical characteristics in the "21.7" henan extremely heavy rainfall event. *Sci. China Earth Sci.*, **65**, https://doi.org/10.1007/s11430-022-9972-9.

Chen, X. C., F. Q. Zhang, and K. Zhao, 2016: Diurnal variations of the land–sea breeze and its related precipitation over South China. *J. Atmos. Sci.*, **73**, 4793–4815, https://doi.org/10.1175/JAS-D-16-0106.1.

Chen, X. C., F. Q. Zhang, and K. Zhao, 2017: Influence of monsoonal wind speed and moisture content on intensity and diurnal variations of the mei-yu season coastal rainfall over South China. *J. Atmos. Sci.*, **74**, 2835–2856, https://doi.org/10.1175/JAS-D-17-0081.1.

Davis, C. A., and T. J. Galarneau Jr., 2009: The vertical structure of mesoscale convective vortices. *J. Atmos. Sci.*, **66**, 686–704, https://doi.org/10.1175/2008JAS2819.1.

Davis, C. A., and W.-C. Lee, 2012: Mesoscale analysis of heavy rainfall episodes from sowmex/timrex. *J. Atmos. Sci.*, **69**, 521–537, https://doi.org/10.1175/JAS-D-11-0120.1.

Ding, Y. H., 2015: On the study of the unprecedented heavy rainfall in Henan Province during 4–8 August 1975: Review and assessment. *Acta Meteorologica Sinica*, **73**, 411–424. (in Chinese with English abstract)

Ding, Y. H., Z. Y. Cai, and J. S. Li, 1978: A case study on the excessively severe rainstrom in Henan Province, early in August, 1975,. *Chinese Journal of Atmospherica Sciences*,

2(4), 276–289, https://doi.org/10.3878/j.issn.1006-9895.1978.04.02. (in Chinese with English abstract)

Doswell III, C. A., H. E. Brooks, and R. A. Maddox, 1996: Flash flood forecasting: An ingredients-based methodology. *Wea. Forecasting*, **11**, 560–581, https://doi.org/10.1175/1520-0434(1996)011<0560:FFFAIB>2.0.CO;2.

Du, Y., and G. X. Chen, 2019: Heavy rainfall associated with double low-level jets over Southern China. Part II: Convection initiation. *Mon. Wea. Rev.*, **147**, 543–565, https://doi.org/10.1175/MWR-D-18-0102.1.

Fu, S.-M., R.-X. Liu, and J.-H. Sun, 2018: On the scale interactions that dominate the maintenance of a persistent heavy rainfall event: A piecewise energy analysis. *J. Atmos. Sci.*, **75**, 907–925, https://doi.org/10.1175/JAS-D-17-0294.1.

Gilmore, M. S., J. M. Straka, and E. N. Rasmussen, 2004: Precipitation uncertainty due to variations in precipitation particle parameters within a simple microphysics scheme. *Mon. Wea. Rev.*, **132**, 2610–2627, https://doi.org/10.1175/MWR2810.1.

Hersbach, H., and Coauthors, 2020: The ERA5 global reanalysis. *Quart. J. Roy. Meteor. Soc.*, **146**, 1999–2049, https://doi.org/10.1002/qj.3803.

Houze, R. A. Jr., 2004: Mesoscale convective systems. *Rev. Geophys.*, **42**, RG4003, https://doi.org/10.1029/2004RG000150.

Hua, S. F., X. Xu, and B. J. Chen, 2020: Influence of multiscale orography on the initiation and maintenance of a precipitating convective system in North China: A case study. *J. Geophys. Res.*, **125**, e2019JD031731, https://doi.org/10.1029/2019JD031731.

Huang, H., G. F. Zhang, K. Zhao, and S. E. Giangrande, 2017: A hybrid method to estimate specific differential phase and rainfall with linear programming and physics constraints. *IEEE Trans. Geosci. Remote Sens.*, **55**, 96–111, https://doi.org/10.1109/TGRS.2016.2596295.

Iacono, M. J., J. S. Delamere, E. J. Mlawer, M. W. Shephard, S. A. Clough, and W. D. Collins, 2008: Radiative forcing by long-lived greenhouse gases: Calculations with the aer radiative transfer models. *J. Geophys. Res.*, **113**, D13103, https://doi.org/10.1029/2008JD009944.

Joyce, R. J., J. E. Janowiak, P. A. Arkin, and P. P. Xie, 2004: Cmorph: A method that produces global precipitation estimates from passive microwave and infrared data at high spatial and temporal resolution. *Journal of Hydrometeorology*, **5**, 487–503, https://doi.org/10.1175/1525-7541(2004)005<0487:CAMTPG>2.0.CO;2.

Li, J., and Y.-L. Chen, 1998: Barrier jets during TAMEX. *Mon. Wea. Rev.*, **126**, 959–971, https://doi.org/10.1175/1520-0493(1998)126<0959:BJDT>2.0.CO;2.

Liu, X., Y. L. Luo, Z. Y. Guan, and D.-L. Zhang, 2018: An extreme rainfall event in coastal South China during SCMREX-2014: Formation and roles of rainband and echo trainings. *J. Geophys. Res.*, **123**, 9256–9278, https://doi.org/10.1029/2018JD028418.

Luo, L. P., M. Xue, K. F. Zhu, and B. W. Zhou, 2018: Explicit prediction of hail in a long-lasting multicellular convective system in eastern China using multimoment microphysics schemes. *J. Atmos. Sci.*, **75**, 3115–3137, https://doi.org/10.1175/JAS-D-17-0302.1.

Luo, Y. L., Y. Gong, and D.-L. Zhang, 2014: Initiation and organizational modes of an extreme-rain-producing mesoscale convective system along a mei-yu front in East China. *Mon. Wea. Rev.*, **142**, 203–221, https://doi.org/10.1175/MWR-D-13-00111.1.

Luo, Y. L., and Coauthors, 2017: The Southern China monsoon rainfall experiment (SCMREX). *Bull. Amer. Meteor. Soc.*, **98**, 999–1013, https://doi.org/10.1175/BAMS-D-15-00235.1.

Maddox, R. A., C. F. Chappell, and L. R. Hoxit, 1979: Synoptic and meso-α scale aspects of flash flood events. *Bull. Amer. Meteor. Soc.*, **60**, 115–123, https://doi.org/10.1175/1520-0477-60.2.115.

Meng, Z. Y., F. Q. Zhang, P. Markowski, D. C. Wu, and K. Zhao, 2012: A modeling study on the development of a bowing structure and associated rear inflow within a squall line over South China. *J. Atmos. Sci.*, **69**, 1182–1207, https://doi.org/10.1175/JAS-D-11-0121.1.

Miranda, P. M. A., and I. N. James, 1992: Non-linear three-dimensional effects on gravity-wave drag: Splitting flow and breaking waves. *Quart. J. Roy. Meteor. Soc.*, **118**, 1057–1081, https://doi.org/10.1002/qj.49711850803.

Nielsen, E. R., and R. S. Schumacher, 2018: Dynamical insights into extreme short-term precipitation associated with supercells and mesovortices. *J. Atmos. Sci.*, **75**, 2983–3009, https://doi.org/10.1175/JAS-D-17-0385.1.

Nielsen, E. R., and R. S. Schumacher, 2020: Observations of extreme short-term precipitation associated with supercells and mesovortices. *Mon. Wea. Rev.*, **148**, 159–182, https://doi.org/10.1175/MWR-D-19-0146.1.

Olson, J. B., J. S. Kenyon, W. A. Angevine, J. M. Brown, M. Pagowski, and K. Sušelj, 2019: A description of the mynn-edmf scheme and the coupling to other components in WRF-ARW. NOAA. Tech. Memo. OAR. GSD, 61, 37 pp.

Overland, J. E., 1984: Scale analysis of marine winds in straits and along mountainous coasts. *Mon. Wea. Rev.*, **112**, 2530–2534, https://doi.org/10.1175/1520-0493(1984)112<2530:SAOMWI>2.0.CO;2.

Overland, J. E., and N. A. Bond, 1995: Observations and scale analysis of coastal wind jets. *Mon. Wea. Rev.*, **123**, 2934–2941, https://doi.org/10.1175/1520-0493(1995)123<2934:OASAOC>2.0.CO;2.

Raymond, D. J., and H. Jiang, 1990: A theory for long-lived mesoscale convective systems. *J. Atmos Sci*, **47**, 3067–3077, https://doi.org/10.1175/1520-0469(1990)047<3067:ATFLLM>2.0.CO;2.

Schumacher, R. S., 2017: Heavy rainfall and flash flooding. *Oxford Research Encyclopedia of Natural Hazard Science*, **24**, Oxford University Press, https://doi.org/10.1093/acrefore/9780199389407.013.132.

Schumacher, R. S., and R. H. Johnson, 2005: Organization and environmental properties of extreme-rain-producing mesoscale convective systems. *Mon. Wea. Rev.*, **133**, 961–976, https://doi.org/10.1175/MWR2899.1.

Schumacher, R. S., and R. H. Johnson, 2006: Characteristics of U. S. extreme rain events during 1999–2003,. *Wea. Forecasting*, **21**, 69–85, https://doi.org/10.1175/WAF900.1.

Shen, Y., P. Zhao, Y. Pan, and J. J. Yu, 2014: A high spatiotemporal gauge-satellite merged precipitation analysis over China. *J. Geophys. Res.*, **119**, 3063–3075, https://doi.org/10.1002/2013JD020686.

Skamarock, W. C., and Coauthors, 2008: A description of the advanced research WRF version 3. No. NCAR/TN-475+STR, 113 pp, http://dx.doi.org/10.5065/D68S4MVH. https://doi.org/10.5065/D68S4MVH.

Su, T., and G. Q. Zhai, 2017: The role of convectively generated gravity waves on convective initiation: A case study. *Mon. Wea. Rev.*, **145**, 335–359, https://doi.org/10.1175/MWR-D-

16-0196.1.

Sun, J. H., Y. C. Zhang, R. X. Liu, S. M. Fu, and F. Y. Tian, 2019: A review of research on warm-sector heavy rainfall in China. *Adv. Atmos. Sci.*, **36**, 1299–1307, https://doi.org/10.1007/s00376-019-9021-1.

Tewari, M., and Coauthors, 2004: Implementation and verification of the unified NOAH land-surface model in the WRF model. *Proc. 20th Conference on Weather Analysis and Forecasting/16th Conference on Numerical Weather Prediction*, Seattle, WA, US, American Meteorological Society, 11–15.

Trapp, R. J., and M. L. Weisman, 2003: Low-level mesovortices within squall lines and bow echoes. Part II: Their genesis and implications. *Mon. Wea. Rev.*, **131**, 2804–2823, https://doi.org/10.1175/1520-0493(2003)131<2804:LMWSLA>2.0.CO;2.

Trier, S. B., and C. A. Davis, 2002: Influence of balanced motions on heavy precipitation within a long-lived convectively generated vortex. *Mon. Wea. Rev.*, **130**, 877–899, https://doi.org/10.1175/1520-0493(2002)130<0877:IOBMOH>2.0.CO;2.

Trier, S. B., C. A. Davis, and W. C. Skamarock, 2000: Long-lived mesoconvective vortices and their environment. Part II: Induced thermodynamic destabilization in idealized simulations. *Mon. Wea. Rev.*, **128**, 3396–3412, https://doi.org/10.1175/1520-0493(2000)128<3396:LLMVAT>2.0.CO;2.

Trier, S. B., C. A. Davis, D. A. Ahijevych, M. L. Weisman, and G. H. Bryan, 2006: Mechanisms supporting long-lived episodes of propagating nocturnal convection within a 7-day WRF model simulation. *J. Atmos. Sci.*, **63**, 2437–2461, https://doi.org/10.1175/JAS3768.1.

Wang, H., Y. L. Luo, and B. J.-D. Jou, 2014: Initiation, maintenance, and properties of convection in an extreme rainfall event during SCMREX: Observational analysis. *J. Geophys. Res.*, **119**, 13 206–13 232, https://doi.org/10.1002/2014JD022339.

Wang, Q. W., M. Xue, and Z. M. Tan, 2016: Convective initiation by topographically induced convergence forcing over the dabie mountains on 24 June 2010,. *Adv. Atmos. Sci.*, **33**, 1120–1136, https://doi.org/10.1007/s00376-016-6024-z.

Wang, Q. W., Y. Zhang, K. F. Zhu, Z. M. Tan, and M. Xue, 2021: A case study of the initiation of parallel convective lines back-building from the south side of a mei-yu front over complex terrain. *Adv. Atmos. Sci.*, **38**, 717–736, https://doi.org/10.1007/s00376-020-0216-2.

Weisman, M. L., and R. Rotunno, 2004: "A theory for strong long-lived squall lines " revisited. *J. Atmos. Sci.*, **61**, 361–382, https://doi.org/10.1175/1520-0469(2004)061<0361:ATFSLS>2.0.CO;2.

Xia, R. D., and D.-L. Zhang, 2019: An observational analysis of three extreme rainfall episodes of 19–20 July 2016 along the Taihang Mountains in North China. *Mon. Wea. Rev.*, **147**, 4199–4220, https://doi.org/10.1175/MWR-D-18-0402.1.

Xu, X., M. Xue, and Y. Wang, 2015a: Mesovortices within the 8 May 2009 bow echo over the central United States: Analyses of the characteristics and evolution based on Doppler radar observations and a high-resolution model simulation. *Mon. Wea. Rev.*, **143**, 2266–2290, https://doi.org/10.1175/MWR-D-14-00234.1.

Xu, X., M. Xue, and Y. Wang, 2015b: The genesis of mesovortices within a real-data simulation of a bow echo system. *J. Atmos. Sci.*, **72**, 1963–1986, https://doi.org/10.1175/JAS-D-14-0209.1.

Xu, X., M. Xue, Y. Wang, and H. Huang, 2017: Mechanisms of secondary convection within a mei-yu frontal mesoscale convective system in Eastern China. *J. Geophys. Res.*, **122**, 47–64, https://doi.org/10.1002/2016JD026017.

Yang, Y., M. Uddstrom, M. Revell, S. Moore, and R. Turner, 2017: Damaging southerly winds caused by barrier jets in the cook strait and wellington region of New Zealand. *Mon. Wea. Rev.*, **145**, 1203–1220, https://doi.org/10.1175/MWR-D-16-0159.1.

Yin, J. F., H. D. Gu, X. D. Liang, M. Yu, J. S. Sun, Y. X. Xie, F. Li, and C. Wu, 2022: A possible dynamic mechanism for rapid production of the extreme hourly rainfall in Zhengzhou City on 20 July 2021,. *Journal of Meteorological Research*, **36**, 6–25, https://doi.org/10.1007/s13351-022-1166-7.

Zeng, W. X., G. X. Chen, Y. Du, and Z. P. Wen, 2019: Diurnal variations of low-level winds and precipitation response to large-scale circulations during a heavy rainfall event. *Mon. Wea. Rev.*, **147**, 3981–4004, https://doi.org/10.1175/MWR-D-19-0131.1.

Zhang, D. L., Y. H. Lin, P. Zhao, X. D. Yu, S. Q. Wang, H. W. Kang, and Y. H. Ding, 2013: The Beijing extreme rainfall of 21 July 2012: "right results" but for wrong reasons. *Geophys. Res. Letters*, **40**, 1426–1431, https://doi.org/10.1002/grl.50304.

Zhang, M., and D.-L. Zhang, 2012: Subkilometer simulation of a torrential-rain-producing mesoscale convective system in East China. Part I: Model verification and convective organization. *Mon. Wea. Rev.*, **140**, 184–201, https://doi.org/10.1175/MWR-D-11-00029.1.

Zhang, M. R., and Z. Y. Meng, 2019: Warm-sector heavy rainfall in Southern China and its WRF simulation evaluation: A low-level-jet perspective. *Mon. Wea. Rev.*, **147**, 4461–4480, https://doi.org/10.1175/MWR-D-19-0110.1.

Zhang, S. S., and Coauthors, 2020: A modeling study of an atmospheric bore associated with a nocturnal convective system over China. *J. Geophys. Res.*, **125**, e2019JD032279, https://doi.org/10.1029/2019JD032279.

Zhang, X., H. Yang, X. M. Wang, L. Shen, D. Wang, and H. Li, 2021: Analysis on characteristic and abnormality of atmospheric circulations of the July 2021 extreme precipitation in Henan. *Transactions of Atmospheric Sciences*, **44**, 672–687, https://doi.org/10.13878/j.cnki.dqkxxb.20210907001.

Zhang, Y. C., J. H. Sun, and S. M. Fu, 2017: Main energy paths and energy cascade processes of the two types of persistent heavy rainfall events over the Yangtze River–Huaihe River Basin. *Adv. Atmos. Sci.*, **34**, 129–143, https://doi.org/10.1007/s00376-016-6117-8.

Zhang, Y. H., M. Xue, K. F. Zhu, and B. W. Zhou, 2019: What is the main cause of diurnal variation and nocturnal peak of summer precipitation in Sichuan Basin, China? The key role of boundary layer low-level jet inertial oscillations *J. Geophys. Res.*, **124**, 2643–2664, https://doi.org/10.1029/2018JD029834.

Zhou, A., K. Zhao, W.-C. Lee, H. Huang, D. M. Hu, and P. L. Fu, 2020: VDRAS and polarimetric radar investigation of a bow echo formation after a squall line merged with a preline convective cell. *J. Geophys. Res.*, **125**, e2019JD031719, https://doi.org/10.1029/2019JD031719.

Zhu, K., C. Zhang, M. Xue, and N. Yang, 2022: Predictability and skill of convection-permitting ensemble forecast systems in predicting the record-breaking "21•7 " extreme rainfall event in Henan Province, China. *Science China Earth Sciences*, **65**, https://doi.org/10.1007/s11430-022-9961-7.